

Enhancement of the volume refractive index sensing by ROTE and its application on cancer and normal cells discrimination

Aoqun Jian^{a,b}, Mingyuan Jiao^{a,b}, Yixia Zhang^{a,b,c}, Qianwu Zhang^d, Xiaoming Xue^e, Shengbo Sang^{a,b,*}, Xuming Zhang^{f,**}

^a MicroNano System Research Center, College of Information and Computer, Taiyuan University of Technology, Taiyuan 030024, China

^b Key Laboratory of Advanced Transducers and Intelligent Control System of Ministry of Education and Shanxi Province, Taiyuan 030024, China

^c College of Biomedical Engineering, Taiyuan University of Technology, Taiyuan 030024, China

^d Key Laboratory of Specialty Fiber Optics and Optical Access Networks, Shanghai University, Shanghai 200072, China

^e Department of Respiration, Shanxi Hospital of Traditional Chinese Medicine, Taiyuan 030012, China

^f Department of Applied Physics, Hong Kong Polytechnic University, Hung Hom, Kowloon, Hong Kong, China

ARTICLE INFO

Article history:

Received 9 January 2020

Received in revised form 22 June 2020

Accepted 22 June 2020

Available online 23 June 2020

Keywords:

Resonant optical tunneling effect

Optical biosensor

Refractive index sensing

ABSTRACT

A volume refractive index (RI) sensor based on the resonant optical tunneling effect (ROTE) is presented in this study. Compared with the classic volume RI sensing structure, the Fabry-Pérot (FP) etalon, the ROTE structure has a higher figure of merit (FOM) than that of the FP cavity with the same cavity length. The sensitivity of the ROTE structure is almost 20 times as high as that of the FP structure, although the Q value of the ROTE structure is lower than that of the FP etalon. Given the excellent volume RI sensing performance of the ROTE structure, three groups of normal human cells and corresponding cancer cells were tested for discrimination in this paper. According to experimental results, the reflection resonant dips of each type of human cancer cell showed a red shift with respect to corresponding normal cells at the same density. The RI sensor based on the ROTE has broad application prospects in biomedical, drug screening, and early cancer diagnoses.

© 2020 Elsevier B.V. All rights reserved.

1. Introduction

More than 85 % of all cancers originate in the epithelium that lines the internal surfaces of organs throughout the body [1]. Before cancer cells become invasive, the volume of the nucleus becomes larger, and the refractive index (RI) is higher than normal cells due to the increased chromatin. Therefore, the RI of cells has the potential to be an indicator of early-stage cancer cells [2].

Since RI is a fundamental optical property of a material, optical sensors have been widely used for RI measurement [3–5]. Nowadays, some models of RI sensors are based on tilted fiber grating with plasmonic nanocoatings [6,7], hybrid propagating-localized plasmonics [8,9], two-dimensional material and its derivatives [10,11], and whispering gallery microcavities [12,13]. For these methods, the evanescent field that exists in the sub-wavelength

range of the two-medium interface is used to achieve a strong light-matter interaction. The intensity of the evanescent wave decreases exponentially with distance away from the medium interface, indicating only changes near the sample surface can be detected and that samples of certain sizes (e.g., most human cells) cannot be effectively measured. However, in volume RI sensing, the incident light propagates through the analyte, making sufficient contact with the analyte. Some well-known classical methods of volume RI sensing include Fabry-Pérot (FP) etalon [14,15], fiber Bragg grating (FBG) [16], and long period fiber grating (LPG) [17]. The signal of the sample at a low density can be obtained using volume RI measurement without capturing and trapping a single individual cell. However, for samples of low density, traditional volume RI methods cannot be used due to the low resolution.

The resonant optical tunneling effect (ROTE) is an optical concept that was first discovered by Yeh [18] in 1988; Hayashi et al. [19] experimentally verified this optical phenomenon in 1999. Over the years, the ROTE has been used in several optical devices as optical switches [20] and optical accelerometers [21]. In recent years, the ROTE structure has been adopted for the RI sensing application. Liquid RI sensors based on the microfluidic structure/optical fibers have been elaborated and their performances have been theoretic-

* Corresponding author at: MicroNano System Research Center, College of Information and Computer, Taiyuan University of Technology, Taiyuan 030024, China

** Corresponding author.

E-mail addresses: sunboa-sang@tyut.edu.cn (S. Sang), xuming.zhang@polyu.edu.hk (X. Zhang).

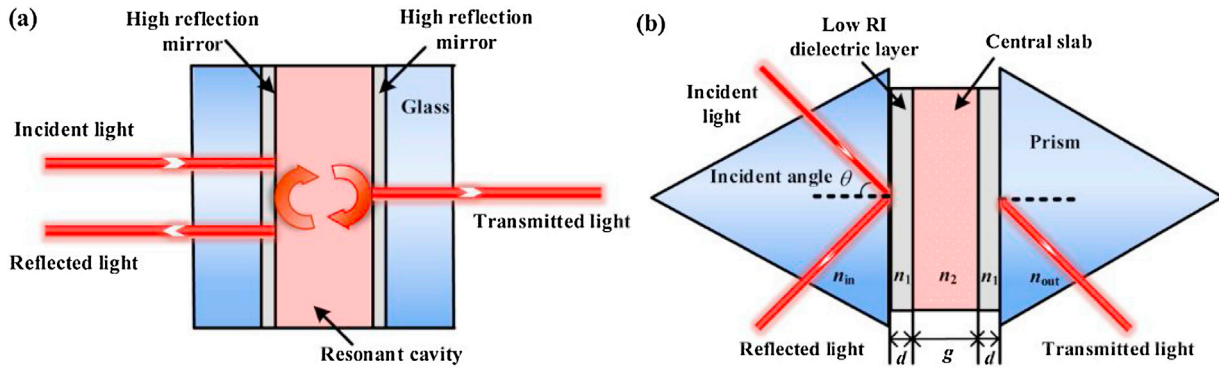


Fig. 1. Schematic diagram of the FP cavity (a) and the ROTE structure (b).

cally analyzed [22,23]. In addition, the high RI sensing capability of the ROTE is first demonstrated by cell density detection [23], and the performance of the designed sensor is among the best.

In this study, the performance of the ROTE sensor is optimized, and new applications are explored. To compare the sensors based on different principles, the sensitivity (S) and Q value of the ROTE and FP structures are simulated by the transfer matrix method (TMM), and the merits of ROTE are clearly revealed compared with the classic FP cavity. Due to the high figure of merit (FOM) of the ROTE structure, the ROTE sensor is applied to the field of cancer/normal cell discrimination. Three types of normal human cells and their corresponding cancer cells are measured in the experiment.

2. Concept and sensor design

Schematic graphs of the FP cavity and ROTE structure are shown in Fig. 1a and 1b, respectively. For the well-known FP cavity, the light resonates in the cavity formed by two highly reflective mirrors. Contrary to the FP etalon, the ROTE is based on the frustrated total internal reflection (FTIR) consisting of five medium layers (input layer, first tunneling gap, central slab, second tunneling gap, and output layer) with a RI distribution of high-low-high-low-high. When the incident angle θ is larger than the critical angle, the tunneled light will resonate in the central slab.

According to our previous studies [22], the change in the RI of the central slab is more sensitive than that of the tunneling gap. Therefore, the central slab of the ROTE structure was selected as the sensing element in the following simulations and experiments. In this study, two K9 triangular prisms form the input and output layers. The polymer layer (MY-131-series) is spin-coated on the triangular prism to form the tunneling gap. The liquid sample ($RI > 1.35$ RIU, refractive index unit) injected between the two tunneling gaps acts as the central cavity (the central slab). In this simulation, the extinction coefficient of the liquid sample (mixing with water and ethanol) is approximately 5×10^{-5} . Therefore, the absorption coefficient of the ROTE cavity is 4 cm^{-1} . The RI of the multi-layer system conforms to the high-low-high-low-high RI distribution. As the ROTE dip is much sharper in S-polarized light than P-polarized light [22], S-polarized light was chosen for better performance. The specific parameters of the ROTE and FP sensing structure are listed in Tables 1 and 2, respectively. To compare the performances of the two sensing structures effectively, the cavity length ($150 \mu\text{m}$) of the two resonates are equal. The K9 glass was chosen as the material for the input medium in the two sensors. The FP sensor uses a 100 nm ($R = 99\%$) thick gold thin layer coated on K9 glass as the high reflectance mirror. The incident angle (61°) of the ROTE was set larger than the total internal reflection angle of 1° and the light was normal incidence in the case of the FP etalon.

3. Performance comparison of FP and ROTE

The sensitivity and Q value are crucial factors in evaluating the RI sensor performance, these parameters were analyzed in simulations using the TMM. Details of the characteristic dip shift due to the RI variation are presented in the ROTE and FP reflection spectra. (Fig. 2a and b, respectively). Both ROTE and FP dips experience a red shift as the RI of the cavity increases. The reflection spectra of the ROTE structure and FP cavity are plotted in Fig. 2c, which reveals the difference between the two sensing structures. The wavelength shift produced by the ROTE sensor is much more significant than that of the FP etalon in response to the same RI change. The sensitivities of the ROTE structure and the FP etalon are compared in Fig. 2d. The sensitivity of the ROTE structure ($24,800 \text{ nm/RIU}$) is 20 times higher than that of the FP structure (1200 nm/RIU). The Q value of the characteristic dip is also significant for the sensing performance. The comparison of Q values of the ROTE and FP is presented in Fig. 2e. With the increased cavity length, the Q value of the FP cavity ($9026 - 12,750$) is 13 times larger than that of the ROTE structure ($700 - 880$). As a sensor, it requires a high FOM to demonstrate its high resolution performance [24,25], which is defined as:

$$\text{FOM} = S * Q/\lambda \quad (1)$$

In Fig. 2f, the ROTE structure has a larger FOM value (approximately 1.5 times), and the difference in FOM of these two structures decreased slightly with the increased cavity length.

According to Gansch et al. [26], the Q value of the resonator can be written as follows:

$$1/Q_{\text{total}} = 1/Q_{\text{str}} + 1/Q_{\text{abs}} + 1/Q_{\text{rad}} \quad (2)$$

where Q_{total} is directly obtained from the experimentally measured spectrum, Q_{str} originates from the loss of refraction and reflection in the structure and is obtained by the simulation without considering the material absorption of the central slab, Q_{abs} accounts for the material absorption and can be determined from comparison of these two simulation results (reflection spectra with/without material absorption of the central slab), and Q_{rad} is the Q value due to the coupling loss of incident light in the experiment and is generated by a comparison of the differences between the experimental and the simulation spectra. As seen in Fig. 3a, the Q_{str} of the ROTE structure ($38,541$) is 1.5 times higher than that of the FP cavity ($25,694$) without considering the material absorption of the central slab. In addition, the resonant depth of the ROTE can reach 0.1 , which is much larger than that of the FP. However, if the material absorption is introduced in the simulation, the width of the ROTE dip is larger than that of the FP. This is possible because the tilted light path of the ROTE has a stronger light-analyte interaction, which also indicates its higher sensitivity and lower Q value. Fig. 3b shows a comparison of the ROTE dips of different polarization states

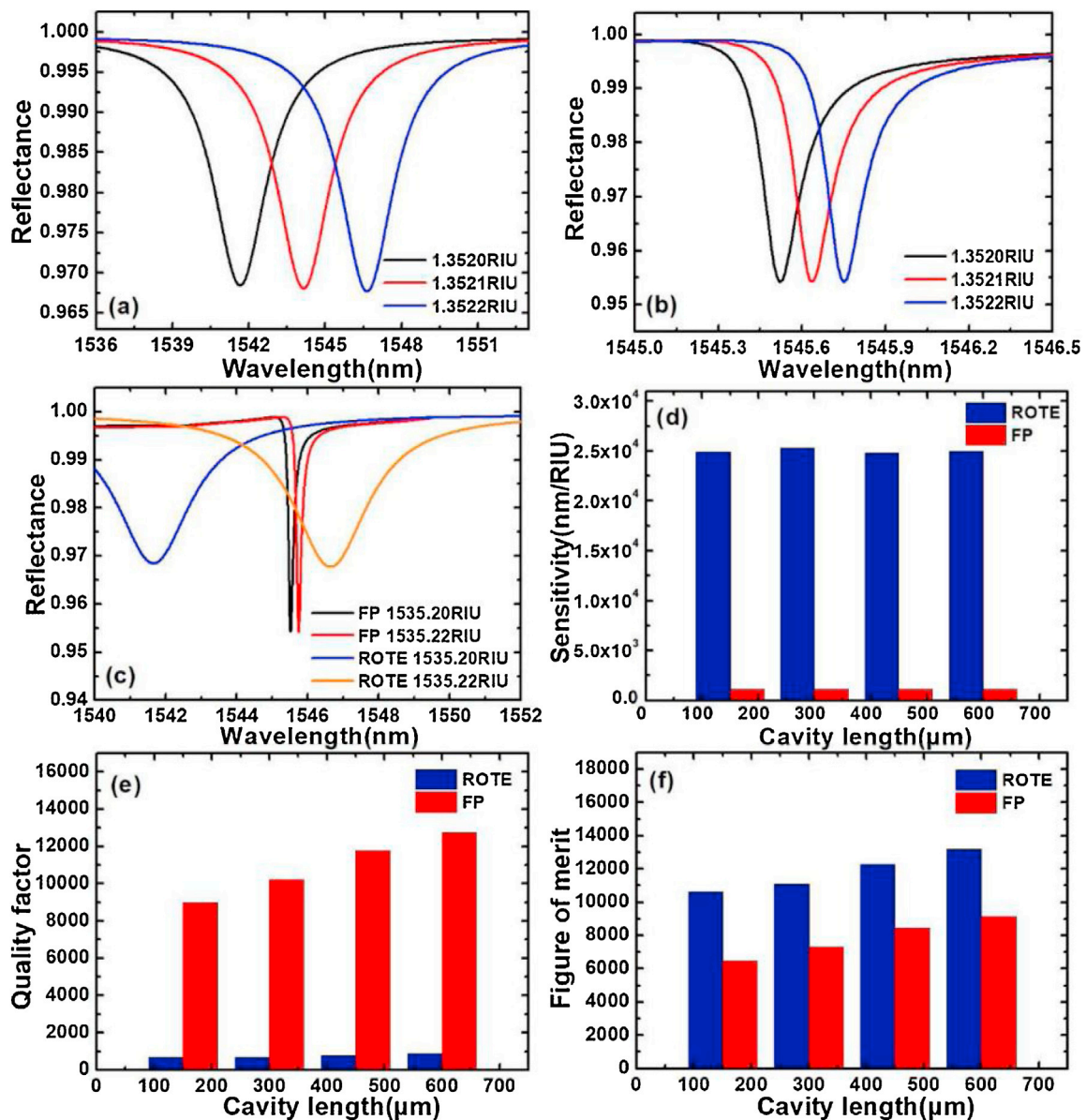
Table 1

Parameters of the ROTE structure.

Parameter	Material	Symbol	Value
RI of input and output layers	K9 glass	n_{in}, n_{out}	$1.59-9.84 \times 10^{-9}i$
RI of the tunneling gaps	MY-131-series	n_1	$1.308-5 \times 10^{-6}i$
Width of the tunneling gaps		d	4 μm
RI of central slab	Sample	n_2	$(1.3520-1.3522)-5 \times 10^{-5}i$
Width of central slab		g	150 μm
Incidence angle		θ	61°

Table 2Parameters of the FP cavity ($R = 99\%$).

Parameter	Material	Symbol	Value
RI of input and output layers	K9 glass	n_{in}, n_{out}	$1.59-9.84 \times 10^{-9}i$
RI of high reflection mirrors	Au	n_1	$0.55881-1.0563 \times 10i$
Width of high reflection mirrors		d	100 nm
RI of FP cavity	Sample	n_2	$(1.3520-1.3522)-5 \times 10^{-5}i$
Width of FP cavity		g	150 μm
Incidence angle		θ	0°

**Fig. 2.** Reflection spectra in the 150 μm cavity with the change of the RI of the ROTE (a) and FP (b) central slab. (c) Comparison of the ROTE and FP reflection spectra in the 150 μm cavity. Sensitivity (d), Q value (e), and FOM (f) of ROTE and FP with different cavity lengths.

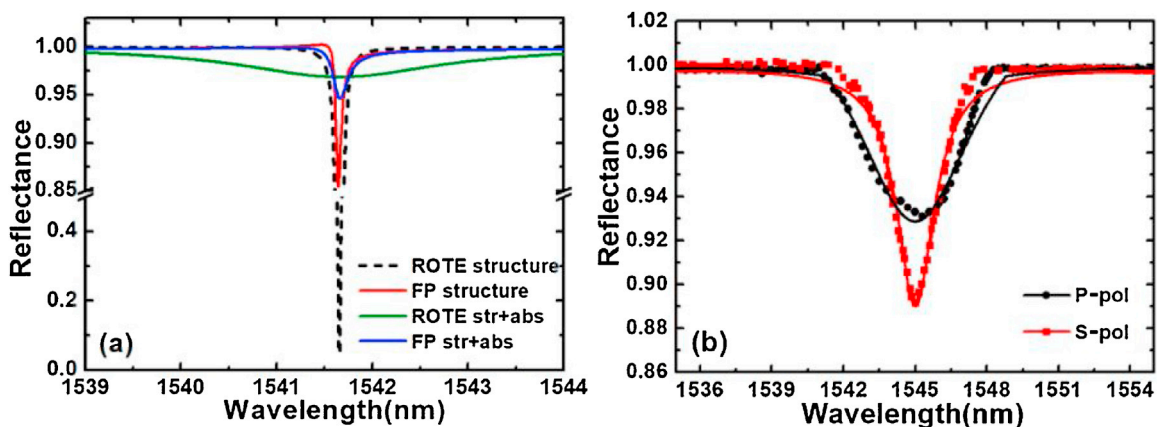


Fig. 3. Comparison of the ROTE and FP reflection spectra with/without absorption (a) and comparison of the reflection spectra of the ROTE for P-polarization and S-polarization (b).

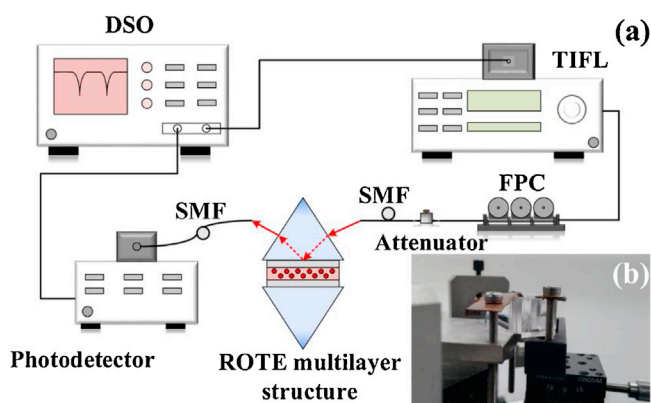


Fig. 4. Experimental setup of the ROTE sensor (a) and photograph of the ROTE structure (b).

(P-polarization and S-polarization). The absorption dip in the S-polarization light is much sharper than that of P-polarization light, which is quite different from the FP etalon. Since both polarization states have the same sensitivity for RI sensing, the S-polarization is adopted in the following experiment for a larger FOM value.

According to theoretical research, the free spectral range (FSR) of the ROTE sensor decreases as the width of the central slab is increased. Therefore, the cavity length of about 200 μm was chosen as the width of the central slab to achieve a larger measurement range.

4. Experiment setup

The experimental setup is shown in Fig. 4. The collimated incident light from a tunable infrared fiber laser (TIFL, New Focus TLB-6700) was irradiated as the input of the system. The polarization state of the laser was adjusted to S-polarized by the fiber polarization controller (FPC) and verified by the polarized beam splitter (PBS, not shown in Fig. 4a). The reflected light was collected by a photodetector (PD, New Focus 1811-FC-AC) and recorded by a digital storage oscilloscope (DSO, GDS-2302A).

The polymer layer is deposited on the prism by spin coating. Before the experiment, the two spin-coated prisms with a thin polymer layer are placed opposite each other and adjusted to be kept in parallel with a specific separation. The gap (about 200 μm) between the two prisms (the central slab) acts as a container for the liquid analyte. Then, the incident angle (61°) was set larger than the total internal reflection angle of 1° and verified by a geometric relation-

ship in the experiment. According to the theoretical research above, when the incident angle and the RI of the central slab are constant, the FSR of the output spectrum is only determined by the width of the central slab. Therefore, when the RI matching liquid (Cargille) was injected into the central slab, the width of the central slab was determined by fitting the reflection spectrum of the system. Before each cell density experiment, the FSR obtained in the measurement was used as a reference for cavity length calibration.

5. Results and discussion

The sensor performance was first demonstrated using the reference solutions. The reference solutions of different RIs were prepared by mixing different volumes of deionized water and anhydrous ethanol for which RIs were measured using a commercial digital RI detector (AR200 digital hand-held refractometer). The experimental results demonstrate that the ROTE absorption dip experiences a red shift as the RI of the central slab increases (as shown in Fig. 5a), and a sensitivity of 19,200 nm/RIU was achieved. In addition, the reference solutions with decreasing RIs are also measured to evaluate the hysteresis effect of the sensor. The wavelength variations of the ROTE dip share almost the same trace for both increasing and decreasing RIs (Fig. 5b).

The errors in measurement originate from three sources: the irradiation heat, mechanical vibration, and the fitting error of the ROTE dip. In the experiment, an optical table was used to isolate the mechanical vibration of the environment as much as possible. Due to the photo-thermal effect, laser irradiation heats the solutions and changes its RI during the experiment. However, the dependence of the wavelength shift on the test time is recorded and such thermal drift is removed in following measurements [23].

To facilitate sample injection into the gap and improve the performance of the sensor, the RI matching liquid was used as the solvent mixed with different cell types for measurement. The red blood cell osmotic fragility test was carried out to prove that cell morphology is not affected by the RI matching liquid. In the experiment, red blood cells were separated from the human blood sample (which was obtained from the technician of this study) by differential centrifugation. The separated red blood cells were washed three times with phosphate buffered saline (PBS, Shanghai Chuang Sai Science and Technology Ltd., China) solution to remove hybrid proteins. Then, the prepared red blood cells were mixed with PBS and the RI matching liquid. After 10 min, the samples were observed under a microscope. Red blood cells in PBS solution exhibited a concentric ring shape and curved features, as shown in Fig. 6a. The morphology of cells did not change in the RI matching liquid,

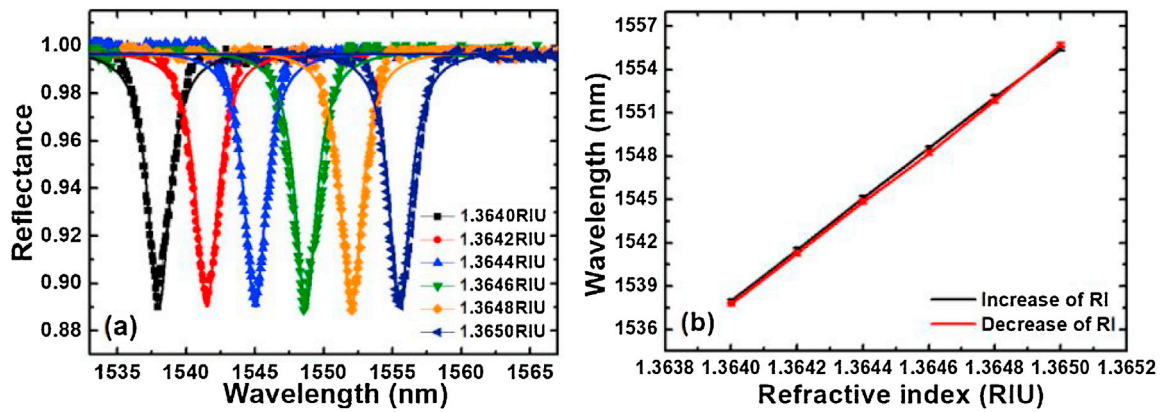


Fig. 5. Red shift of the absorption dip with the RI change of the central slab (a); resonant wavelengths in the different RIs (b). (For interpretation of the references to colour in the Figure, the reader is referred to the web version of this article).

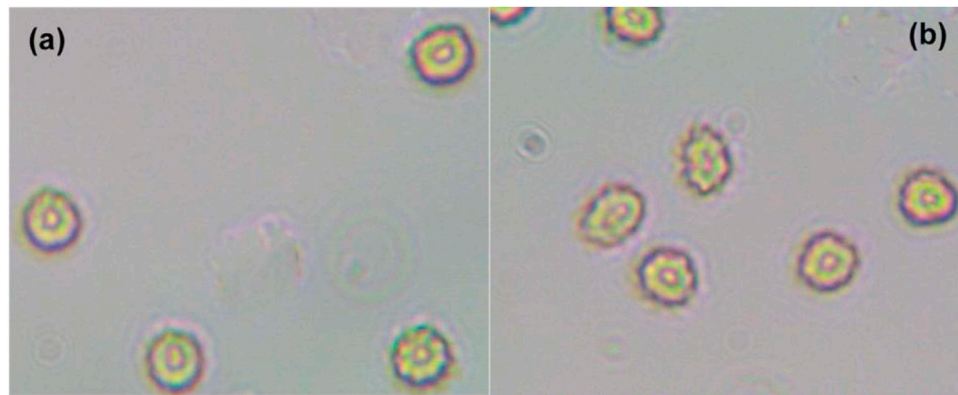


Fig. 6. Microscopic images of (a) red blood cells mixed with PBS solution; and (b) red blood cells mixed with the RI matching liquid. (For interpretation of the references to colour in the Figure, the reader is referred to the web version of this article).

Table 3

Three groups of cells type in the experiment.

	Normal	Cancer
Human gastric cells	GES-1	MGC-803
Human liver cells	LO ₂	7721
Human epidermal cells	HEM	MEL

demonstrating that the RI matching liquid maintains cell morphology during the measurement process.

The capability of the ROTE sensor for discriminating normal and cancer cells was verified using three groups of cells (listed in Table 3). MGC-803, GES-1, LO₂, and 7721 cells were provided by the Cell Bank of the Chinese Academy of Sciences (Shanghai, China). HEM and MEL cells were provided by Shandong University (Shandong, China). Images of these cells are presented in Fig. 7. It is difficult to discriminate between normal and cancer cells based on morphology. Before the experiment, cell counts were determined with a hemocytometer. Each cell type was separated from the cell culture solution by centrifugation and mixed with the RI matching liquid. Cell solutions with three different cell densities (4.48×10^5 , 5.97×10^5 , 7.46×10^5 cells/mL) were prepared for further measurement. The ROTE

reflection spectra of GES-1 and MGC-803 cells at three different cell densities are presented in Fig. 8a. The black curve represents the reflection spectrum of the RI matching liquid, which is a result of the control (blank) experiment. As the cell density increases, the ROTE absorption dip experiences a red shift, and the resonant wavelength of cancer cells is larger than that of normal cells at the same cell

density. With increasing cell density, the red shift of the cancer cells is larger than that of normal cells.

The wavelength shift as the cell density increases is represented as the slopes by linear fitting. When the cell transforms from a normal to cancerous state, the alteration of genomic and proteomic properties affects the RI of cells [27]. The measurement was repeated five times for each sample. As shown in Fig. 8b, cell density is linear with the wavelength of the reflection dip and the error bar represents the distribution of the resonant wavelengths. After each experiment, the central slab is washed carefully with ethanol and thoroughly dried to maintain stable experimental conditions. Following the same procedure, the ROTE reflection spectra of LO₂ and 7721 cells, HEM and MEL cells are shown in Fig. 8c and 8e, respectively. The experimental results are similar to those of the first group. The resonant wavelength versus cell densities is plotted in Fig. 8d and 8f. According to the previous sensor characterization experiment (Fig. 5), the wavelength of the ROTE dip is only dependent on the RI of the central slab when the cavity length is calibrated. Therefore, the RI values of samples can be obtained from the shift of the ROTE dip with respect to the reference wavelength (black curve). The experimental results are summarized and listed in Table 4. Furthermore, the *t*-test was used for statistical analysis at a 95 % confidence interval, $p < 0.05$ showed that the change in wavelength is statistically different for healthy and corresponding cancer cells at the same density. The experimental results are consistent with previous RI measurements of healthy and cancer cells [28,29].

It is to be noted that, the reference solutions (mixing different volumes of deionized water and anhydrous ethanol) with different

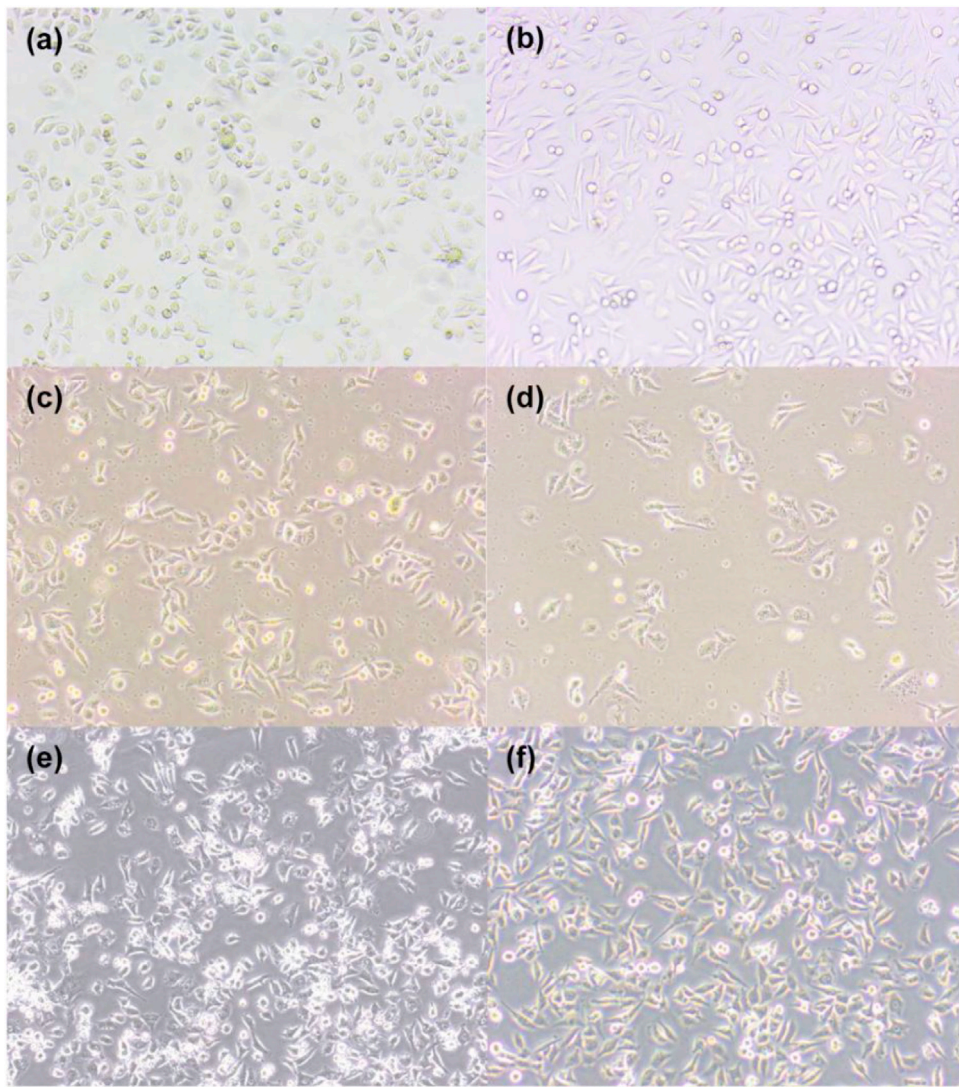


Fig. 7. Images of microscope (a) GES-1 cells; (b) MGC-803 cells; (c) LO₂ cells; (d) 7721 cells; (e) HEM cells; (f) MEL cells.

Table 4

The RI of different cell types at different cell densities.

Type	Density(cells/mL)	RI value(RIU)	Error(RIU)	Slope of the fitting linear
GES-1	4.48×10^5	1.65998	$\pm 2.7 \times 10^{-5}$	2.03801×10^{-6}
	5.97×10^5	1.66009	$\pm 2.6 \times 10^{-5}$	
	7.46×10^5	1.66020	$\pm 2.9 \times 10^{-5}$	
MGC-803	4.48×10^5	1.66104	$\pm 2.7 \times 10^{-5}$	4.41027×10^{-6}
	5.97×10^5	1.66126	$\pm 2.6 \times 10^{-5}$	
	7.46×10^5	1.66149	$\pm 2.8 \times 10^{-5}$	
LO ₂	4.48×10^5	1.66013	$\pm 2.3 \times 10^{-5}$	2.72784×10^{-6}
	5.97×10^5	1.66026	$\pm 2.7 \times 10^{-5}$	
	7.46×10^5	1.66040	$\pm 2.6 \times 10^{-5}$	
7721	4.48×10^5	1.66069	$\pm 2.6 \times 10^{-5}$	3.87328×10^{-6}
	5.97×10^5	1.66088	$\pm 2.5 \times 10^{-5}$	
	7.46×10^5	1.66109	$\pm 2.6 \times 10^{-5}$	
HEM	4.48×10^5	1.66034	$\pm 2.7 \times 10^{-5}$	3.092×10^{-6}
	5.97×10^5	1.66052	$\pm 2.5 \times 10^{-5}$	
	7.46×10^5	1.66067	$\pm 2.8 \times 10^{-5}$	
MEL	4.48×10^5	1.66124	$\pm 3.1 \times 10^{-5}$	5.02691×10^{-6}
	5.97×10^5	1.66154	$\pm 2.8 \times 10^{-5}$	
	7.46×10^5	1.66179	$\pm 2.9 \times 10^{-5}$	

RI is adopted for the sensor performance evaluation. However, for the cell experiments, in order to maintain the original morphology of the cells, the RI matching liquid is utilized as a solvent to prepare the cell solutions. As the surface tension of the RI matching

liquid is smaller than those of the reference solutions, the separation between the two prisms (the central slab of the ROTE) in the cell experiments is narrowed to prevent the leakage during the measurement. Because the cavity lengths are different in the sen-

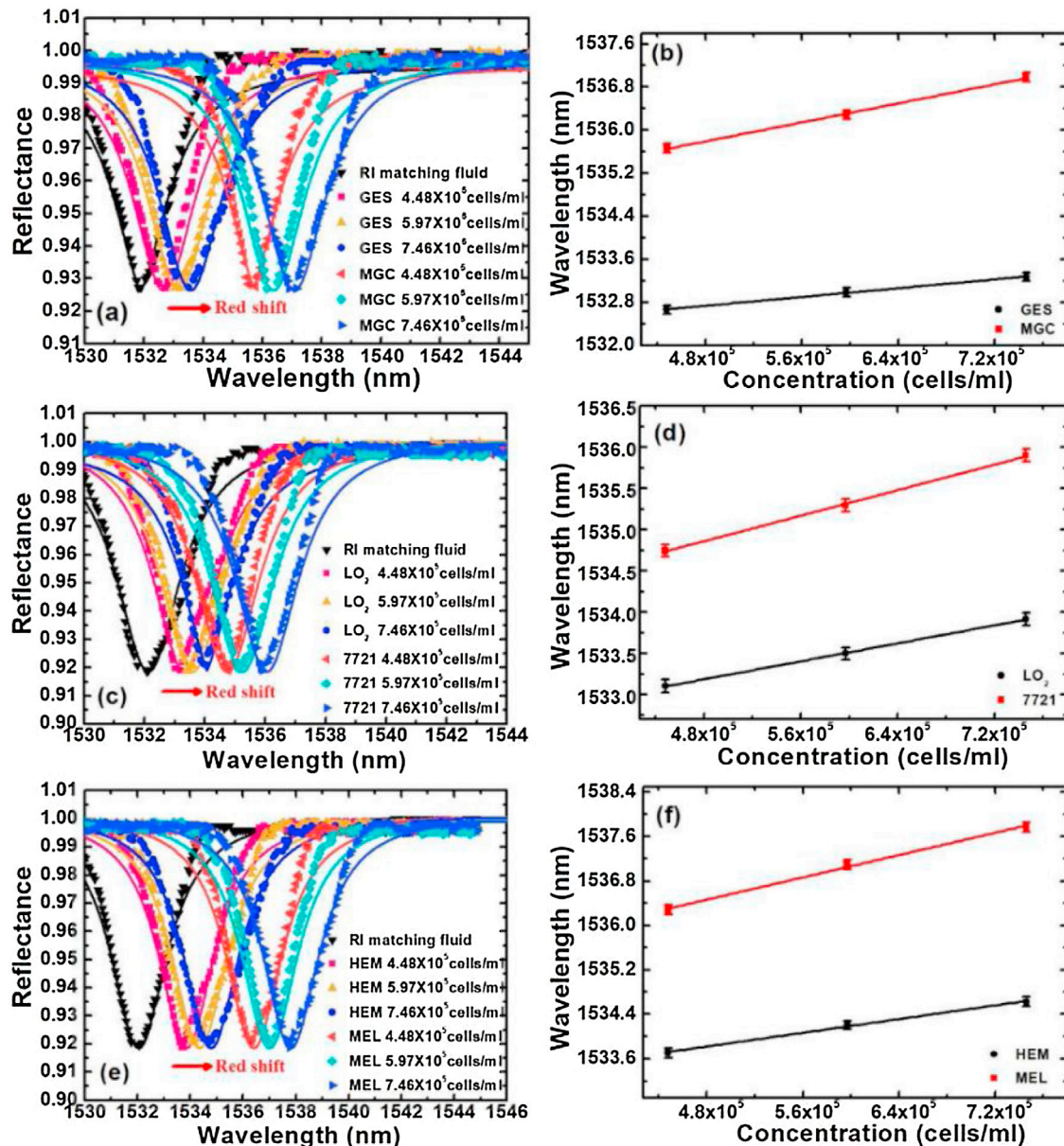


Fig. 8. The ROTE dip presents a red shift as the cell density of (a) GES-1 and MGC-803 cells; (c) LO_2 and 7721 cells; and (e) HEM and MEL cells change. (b), (d), and (f) Dependence of the ROTE resonant wavelength on different cell densities. (For interpretation of the references to colour in the Figure, the reader is referred to the web version of this article).

sor characterization and cell experiments, different RI values can be observed for the same resonant wavelength (e.g. in the case of the generated dip centered around 1536 nm, RI values around 1.3639 and 1.6613 have been derived in sensor characterization test and the experiment of MGC-803 cell, respectively) However, because the RI values of samples can be obtained from the shift of the ROTE dip with respect to the calibration wavelength, this phenomenon will not hinder the application of our sensor.

6. Conclusions

In this study, a novel volume RI sensing method based on the ROTE has been proposed. Compared with the FP classic etalon, a 20-fold higher sensitivity can be achieved by adopting the ROTE structure. As a result of the strong light-analyte interaction, the

Q value of the ROTE structure is lower than that of the FP cavity. However, in the case of FOM, an important parameter has been proposed to evaluate the performance of sensors; the ROTE structure is 1.5 times higher than that of the classic volume RI sensing structure. Due to its outstanding sensing performance, the discrimination between normal and corresponding cancer cells can be achieved at low cell densities, as shown with GES-1, MGC-803, LO_2 , 7721, HEM, and MEL cells. The optical responses of healthy and corresponding cancer cells were significantly different in the experiment. Changes in the biochemical and physiological properties of cells as they progress from healthy to a cancerous state result in an optical response change. To discriminate between normal and corresponding cancer cells, the ROTE sensor is label-free, fast, and highly-sensitive compared with other detection techniques. This sensor may be useful for drug screens, cellular physiological or pathological analyses, and early cancer diagnoses.

Funding

This study was financially supported by the National Natural Science Foundation of China (No. 61971301, 61471255, 61474079, 51622507, 81602506 and 61377068), 863 project (2015AA042601), Excellent Talents Technology Innovation Program of Shanxi Province (201805D211021), and Research Grants Council of Hong Kong (N.PolyU505/13, 152184/15E, 152127/17E and 152126/18E).

Disclosures

The authors declare that there are no conflicts of interest related to this article.

CRediT authorship contribution statement

Aoqun Jian: Conceptualization, Writing - original draft. **Mingyuan Jiao:** Investigation, Writing - original draft. **Yixia Zhang:** Formal analysis. **Qianwu Zhang:** Resources. **Xiaoming Xue:** Resources. **Shengbo Sang:** Funding acquisition. **Xuming Zhang:** Writing - review & editing.

Declaration of Competing Interest

The authors declare that there are no conflicts of interest related to this article.

References

- [1] V. Backman, M.B. Wallace, L. Perelman, J. Arendt, R. Gurjar, M. Müller, et al., Detection of preinvasive cancer cells, *Nature* 406 (2000) 35–36.
- [2] N. Ayyanar, G.T. Raja, M. Sharma, D.S. Kumar, Photonic crystal fiber-based refractive index sensor for early detection of cancer, *IEEE Sens. J.* 18 (2018) 7093–7099.
- [3] C. Ciminelli, C.M. Campanella, F. Dell’Olio, C.E. Campanella, M.N. Armenise, Label-free optical resonant sensors for biochemical applications, *Prog. Quantum Electron.* 37 (2013) 51–107.
- [4] X. Fan, I.M. White, Optofluidic microsystems for chemical and biological analysis, *Nat. Photonics* 5 (2011) 591–597.
- [5] Y. Xu, P. Bai, X. Zhou, Y. Akimov, C.E. Png, L.K. Ang, et al., Optical refractive index sensors with plasmonic and photonic structures: promising and inconvenient truth, *Adv. Opt. Mater.* 7 (2019), 1801433.
- [6] T. Guo, F. Liu, X. Liang, X. Qiu, Y. Huang, C. Xie, et al., Highly sensitive detection of urinary protein variations using tilted fiber grating sensors with plasmonic nanocoatings, *Biosens. Bioelectron.* 78 (2016) 221–228.
- [7] J.-M. Renoirt, C. Zhang, M. Debligny, M.-G. Olivier, P. Mégret, C. Caucheteur, High-refractive-index transparent coatings enhance the optical fiber cladding modes refractometric sensitivity, *Opt. Express* 21 (2013) 29073–29082.
- [8] N. Vasilantonakis, G. Wurtz, V. Podolskiy, A. Zayats, Refractive index sensing with hyperbolic metamaterials: strategies for biosensing and nonlinearity enhancement, *Opt. Express* 23 (2015) 14329–14343.
- [9] F. Abbas, M. Faryad, A highly sensitive multiplasmonic sensor using hyperbolic chiral sculptured thin films, *J. Appl. Phys.* 122 (2017), 173104.
- [10] V. Kravets, R. Jalil, Y.-J. Kim, D. Ansell, D. Aznakyeva, B. Thackray, et al., Graphene-protected copper and silver plasmonics, *Sci. Rep.* 4 (2014) 5517.
- [11] Q. Ouyang, S. Zeng, L. Jiang, J. Qu, X.-Q. Dinh, J. Qian, et al., Two-dimensional transition metal dichalcogenide enhanced phase-sensitive plasmonic biosensors: theoretical insight, *J. Phys. Chem. C* 121 (2017) 6282–6289.
- [12] Y. Zhi, X.C. Yu, Q. Gong, L. Yang, Y.F. Xiao, Single nanoparticle detection using optical microcavities, *Adv. Mater.* 29 (2017), 1604920.
- [13] Y.-L. Chen, W.-L. Jin, Y.-F. Xiao, X. Zhang, Measuring the charge of a single dielectric nanoparticle using a high-Q optical microresonator, *Phys. Rev. Appl.* 6 (2016), 044021.
- [14] D.R. Ramasawmy, E. Martin, J.A. Guggenheim, E.Z. Zhang, P.C. Beard, B.E. Treeby, et al., Analysis of the directivity of glass-etalon Fabry–Pérot ultrasound sensors, *IEEE Trans. Ultrason. Ferroelectr. Freq. Control* 66 (2019) 1504–1513.
- [15] E.J. Jung, W.-J. Lee, M.J. Kim, S.H. Kwang, B.S. Rho, Air cavity-based Fabry–Pérot interferometer sensor fabricated using a sawing technique for refractive index measurement, *Opt. Eng.* 53 (2014), 017104.
- [16] A. Iadicco, A. Cusano, A. Cutolo, R. Bernini, M. Giordano, Thinned fiber Bragg gratings as high sensitivity refractive index sensor, *IEEE Photonics Technol. Lett.* 16 (2004) 1149–1151.

- [17] Z. He, F. Tian, Y. Zhu, N. Lavlinskaia, H. Du, Long-period gratings in photonic crystal fiber as an optofluidic label-free biosensor, *Biosens. Bioelectron.* 26 (2011) 4774–4778.
- [18] P. Yeh, M. Hendry, Optical waves in layered media, *Phys. Today* 43 (1990) 77.
- [19] S. Hayashi, H. Kurokawa, H. Oga, Observation of resonant photon tunneling in photonic double barrier structures, *Opt. Rev.* 6 (1999) 204–210.
- [20] N. Yamamoto, K. Akahane, S.-I. Gozu, N. Ohtani, All-optical control of the resonant-photon tunneling effect observed in GaAs/AlGaAs multilayered structures containing quantum dots, *Appl. Phys. Lett.* 87 (2005), 231119.
- [21] A. Jian, C. Wei, L. Guo, J. Hu, J. Tang, J. Liu, et al., Theoretical analysis of an optical accelerometer based on resonant optical tunneling effect, *Sensors* 17 (2017) 389.
- [22] A. Jian, X. Zhang, W. Zhu, M. Yu, Optofluidic refractometer using resonant optical tunneling effect, *Biomicrofluidics* 4 (2010), 043008.
- [23] A. Jian, L. Zou, G. Bai, Q. Duan, Y. Zhang, Q. Zhang, et al., Highly sensitive cell concentration detection by resonant optical tunneling effect, *J. Lightw. Technol.* 37 (2019) 2800–2806.
- [24] B. Gao, Y. Wang, T. Zhang, Y. Xu, A. He, L. Dai, et al., Nanoscale refractive index sensors with high figures of merit via optical slot antennas, *ACS Nano* 13 (2019) 9131–9138.
- [25] Z. Zhang, J. Yang, X. He, J. Zhang, J. Huang, D. Chen, et al., Plasmonic refractive index sensor with high figure of merit based on concentric-rings resonator, *Sensors* 18 (2018) 116.
- [26] R. Gansch, S. Kalchmair, P. Genevet, T. Zederbauer, H. Detz, A.M. Andrews, et al., Measurement of bound states in the continuum by a detector embedded in a photonic crystal, *Light Sci. Appl.* 5 (2016), e16147.
- [27] L.-W. Yuan, H. Yamashita, Y. Seto, Glucose metabolism in gastric cancer: the cutting-edge, *World J. Gastroenterol.* 22 (2016) 2046.
- [28] S. Jindal, S. Sobti, M. Kumar, S. Sharma, M.K. Pal, Nanocavity-coupled photonic crystal waveguide as highly sensitive platform for cancer detection, *IEEE Sens. J.* 16 (2016) 3705–3710.
- [29] H. Chopra, R.S. Kaler, B. Painam, Photonic crystal waveguide-based biosensor for detection of diseases, *J. Nanophoton.* 10 (2016), 036011.

Biographies

Aoqun Jian received the B.Eng. degree in electronic and information technology and the M.Eng. degree in microelectronics and solid electronics from the North University of China, Taiyuan, China, in 2005 and 2008, respectively. He received the Ph.D. degree in the Department of Applied Physics, The Hong Kong Polytechnic University, Kowloon, Hong Kong, in 2013. His current research interests include nanooptics, particularly surface plasmon resonance resonant, optical tunneling effect and optofluidics.

Mingyuan Jiao received the B.Eng. degree in optical information sciences and technology from Shanxi Datong University, Datong, China, in 2016. He is now pursuing the M.Eng. degree in electronics science and technology from Taiyuan University of Technology Taiyuan, China. His current research interests include biosensors, resonant optical tunneling effect and waveguide structure.

Yixia Zhang received Doctor Science degree in Biomedical Engineering from Shanghai Jiao Tong University, Shanghai, China. Her current research interests include NPs biological synthesis. The project she presided over is prewarning early stage cancer by breath based on VOC s biomarker.

Qianwu Zhang received his PhD in communication and information engineering from Shanghai University in 2015. In 2015, he rejoined Shanghai University as a lecturer. His research interests are focused on optical amplifiers, optical transceivers, optical and electrical signal processing, high-speed optical signal transmission in long-haul, metropolitan, and access networks.

Xiaoming Xue received Master of Medicine degree from Fujian University of Traditional Chinese Medicine, Fuzhou, China, in 2006. He received Doctor of Medicine degree from Hubei University of Traditional Chinese Medicine in 2012. Now he is a chief physician of the Respiratory Department of Chinese Traditional Medicine Hospital in Shanxi Province.

Shengbo Sang received the B.Eng. degree in communication engineering and the M.Eng. degree in electronic science and technology from the North University of China, Taiyuan, China, in 2000 and 2006, respectively. He received the Ph.D. degree from the school of mechanical engineering, Ilmenau, Ilmenau University of Technology, Germany, in 2010. His current research interests include MEMS/NEMS, optical devices and biosensors.

Xuming Zhang received the B.Eng. degree in precision mechanical engineering from the University of Science and Technology of China, Hefei, China, in 1994, and the Ph.D. degree from the School of Electrical and Electronic Engineering, Nanyang Technological University, Singapore, in 2006. He is currently an Associate Professor with the Department of Applied Physics, Hong Kong Polytechnic University, Hong Kong. His current research interests include microelectromechanical system, microfluidics, sensors, and photocatalysis.